Whole-brain mapping reveals the divergent impact of ketamine on the dopamine system

Malika S. Datta[1,2,#], Yannan Chen[1,3,#], Shradha Chauhan[1], Jing Zhang[1], Estanislao Daniel De La Cruz[1], Cheng Gong[1,3], Raju Tomer[1,2,3,*]

[1]Department of Biological Sciences

[2]Mortimer B. Zuckerman Mind Brain and Behavior Institute

[3]Department of Biomedical Engineering

Columbia University

*Corresponding author: raju.tomer@columbia.edu

[#]These authors contributed equally to this work

Abstract

Ketamine is a multifunctional drug with clinical applications as an anesthetic, as a pain management medication and as a transformative fast-acting antidepressant. It is also abused as a recreational drug due to its dissociative property. Recent studies in rodents are revealing the neuronal mechanisms that mediate the complex actions of ketamine, however, its long-term impact due to prolonged exposure remains much less understood with profound scientific and clinical implications. Here, we develop and utilize a high-resolution whole-brain phenotyping approach to show that repeated ketamine administration leads to a dosage-dependent decrease of dopamine (DA) neurons in the behavior state-related midbrain regions and, conversely, an increase within the hypothalamus. Congruently, we show divergently altered innervations of prefrontal cortex, striatum, and sensory areas. Further, we present supporting data for the post-transcriptional regulation of ketamine-induced structural plasticity. Overall, through an unbiased whole-brain analysis, we reveal the divergent brain-wide impact of chronic ketamine exposure on the association and sensory pathways.

Keywords: Dopamine, Ketamine, Plasticity, Whole brain, neural circuit adaptations, modulation

INTRODUCTION

Ketamine is a schedule III (US Food and Drug Administration) substance with clinical applications as a dissociative anesthetic, as a pain management drug and, most recently, as a transformative fast-acting antidepressant[1–6]. Pharmacologically, ketamine is thought to act broadly in the brain[7], most prominently as a non-competitive antagonist of the N-methyl-D-aspartate receptor (NMDAR)[8,9] but also as a blocker of hyperpolarization-activated cyclic nucleotide (HCN1)[10,11] channels and as a potential activator of opioid receptors[12,13]. Recent studies in rodent models are unraveling the cellular and neural circuit underpinnings of ketamine's complex action in the brain. For example, an antidepressant dose of ketamine was shown to promote spinogenesis and synaptogenesis in prefrontal cortical circuits to rescue the eliminated spines in a depression mouse model[14]. Another recent study showed that sub-hypnotic doses (50 and 100 mg/kg) of ketamine switches the spontaneous excitatory activity across the neocortex by suppressing the active neurons while activating the previously silent neurons, paralleling its dissociative property[15]. Acute ketamine administration also broadly impacts the dopaminergic modulatory system (via NMDAR antagonism[16,17]), resulting in increased firing in the ventral tegmental area (VTA) dopamine (DA) neurons and enhanced DA release in the frontal cortex, striatum and nucleus accumbens[16–18] (**Fig. 1a**).

In contrast, the long-term impact of chronic ketamine exposure on brain networks remains much less understood, with profound scientific and clinical implications[19,20]. The antidepressant effect of ketamine is known to be transient, especially in treatment-resistant depression patients, thus often requiring maintenance treatments over years[19]. Additionally, the long-term recreational abuse has been associated with cognitive and sensory impairments[21–23] and significant damages have been reported in the frontal, parietal, and occipital cortices in the brain[24]. Recent studies in mice have further revealed significant alterations in neocortical microcircuit synchrony after repeated exposure to ketamine[25,26]. Therefore, with its broad clinical importance and increasing long-term abuse potential at higher doses, there is a considerable interest in understanding the molecular, cellular, and neural circuit alterations caused by long-term exposure to ketamine over a wide range of doses[19,20].

We sought to systematically investigate the brain-wide impact of chronic (*R,S*)-ketamine exposure on the entire dopaminergic system in mice. By utilizing a range of sub-hypnotic[15] doses

65 (30 and 100 mg/kg) and high-resolution whole-brain phenotyping of DA neurons, we show that
66 chronic ketamine exposure over time results in divergent brain-wide changes in the DA neuron
67 populations and their long-range projections to the prefrontal cortex and sensory areas. Further,
68 we reveal the role of post-transcriptional regulation mechanisms in modulating the ketamine-
69 induced structural plasticity in the DA system. Overall, through an unbiased whole-brain high-
70 resolution mapping, we reveal the broad non-monotonic impact of ketamine on the brain-wide DA
71 modulatory system.

72 **RESULTS**

73 **High-resolution whole-brain phenotyping of ketamine-treated animals**

74 We established a complete pipeline for whole-brain labeling, high-resolution imaging and
75 comparative phenotyping of the entire dopaminergic modulatory system after 1, 5 and 10 days of
76 daily (*R,S*)-ketamine (30 and 100 mg/kg) and saline control intraperitoneal (i.p.) injections (**Fig.**
77 **2**). The cellular toxicity of the ketamine exposure was assessed by α-activated caspase antibody
78 staining after 10 days of 100 mg/kg daily i.p. injections, revealing no significant cell death in the
79 brain (**Supplementary Fig. 1**). The locomotion of injected animals was video-recorded and
80 quantified at 15' and 60' post injections (**Supplementary Fig. 2**). The 30 mg/kg group, but not
81 100 mg/kg, exhibited increasing (with days of exposure) locomotion sensitivity 15'-post injection.

82 The extracted intact brains were stained with α-tyrosine hydroxylase (TH; rate-limiting
83 enzyme for DA synthesis), which is a widely used marker of DA neurons[27] (**Fig. 2,**
84 **Supplementary Video 1**). Note that even though DA may further get converted to other
85 catecholamines (norepinephrine and/or epinephrine) in the downstream pathways, the distribution
86 of these noradrenergic neurons is very well characterized and known to be localized within the
87 hindbrain regions (pons and medulla)[28,29]. Nevertheless, due to their brain-wide projections (e.g.,
88 to cerebral cortex, hippocampus, amygdala and hypothalamus), the precise identity of the TH+
89 neuronal projections (as DA or noradrenergic) may only be inferred as catecholaminergic[28,29].

90 For investigating the TH mRNA expression, we established and used a whole-brain
91 staining method based on hybridization chain reaction[30,31], and also utilized a well-characterized
92 inducible Cre line, TH-CreER[32], crossed with a tdTomato reporter line (**Supplementary Fig. 3**).
93 The intact brain samples were cleared with either iDISCO+[33] or passive CLARITY[34] methods, and
94 imaged at high-resolution with COLM[34] or light sheet theta microscopy (LSTM[35]) (**Fig. 2**).

95 Finally, we developed a set of accurate large data analysis methods (suiteWB, **Fig. 2b**) for
96 high-resolution phenotyping of the entire dopaminergic system – both at the levels of TH+ cell
97 bodies as well as TH+ brain-wide projections (**Fig. 2b**). To this end, we first generated a local
98 average reference (from 7 brains), which was annotated by the registration of Allen brain atlas
99 (ABA, ccfv3[36]) annotations. In addition, we developed a multi-model image segmentation
100 approach to accurately detect the TH+ cell bodies and their brain-wide projections (**Fig. 2b,**
101 **Supplementary Video 3**). ANOVA and two-sided Mann Whitney U tests with Bonferroni
102 correction were utilized for statistical comparisons. Overall, suiteWB methods allow accurate
103 high-resolution phenotyping of the brain-wide structural plasticity.

104 **Dosage-dependent divergent impact of chronic ketamine exposure on the DA domains**

105 We generated high-resolution whole-brain maps of TH+ neurons after 1, 5, and 10 days of
106 daily ketamine and saline i.p. injections (**Fig. 3, Supplementary Video 3**). Using suiteWB, TH+
107 neuron counts were calculated across all the brain regions (**Fig. 3a**) and were statistically compared
108 across treatment groups at multiple scales by utilizing different graph-cut levels of the hierarchical
109 ABA annotation tree. Robust, statistically significant alterations were only detected after 10 days
110 of ketamine exposure for both 30 and 100 mg/kg ketamine treatment groups, therefore, 1- and 5-
111 days treatment datasets were not analyzed further. In addition, as expected, 100 mg/kg treatment
112 group exhibited much more changes than the 30 mg/kg treatment group (**Fig. 3**).

113 At a higher-level annotation (i.e., larger brain regions ROIs; level 6), we found an overall
114 dose-dependent statistically significant decrease in TH+ neuron counts within the behavior-state
115 related mid-brain regions (MBsta) and, conversely, an overall increase within the hypothalamic
116 lateral zone (LZ) in both the 30 and 100 mg/kg (10 days) treatment groups (**Fig. 3a**). In addition,
117 for the 100 mg/kg group, we observed a tendency for increase within the hypothalamic
118 periventricular zone (PVZ) and, for the 30 mg/kg group, significant decrease within the
119 periventricular region (PVR) (**Fig. 3a**). Next, we compared the brains at lower-level (level 8) graph
120 cut of the ABA annotation tree. For both 30 and 100 mg/kg treatment groups, we observed a robust
121 decrease in the dorsal raphe (DR[37]) and increase in the lateral hypothalamic region zona incerta
122 (ZI[38]). In addition, in the 100 mg/kg treatment group, we observed a robust decrease in the reticular
123 nucleus retrorubral area (RR[39]) and increases in the arcuate hypothalamic nucleus (ARH[40]), the
124 periventricular hypothalamic nucleus posterior part (PVp), tuberomammillary nucleus (TM) and

125 the periventricular hypothalamic nucleus descending division (PVHd) (**Fig. 3a**). Whereas, in the
126 30 mg/kg treatment group, we found significant increases in mid-brain region SNr (Substantia
127 nigra reticular part) and a significant decrease in the dorsomedial nucleus of the hypothalamus
128 (DMH) and the medial hypothalamic region MPN[41] (preoptic nucleus). These brain-wide
129 alterations were further validated by an independent voxels-based (20x20x20 μm^3 sampling) brain
130 parcellation approach (**Fig. 3b**). Representative example volume renderings are shown for RR,
131 DR, ARH, PVp and PVHd (**Fig. 3c**, 100 mg/kg ketamine-treated group).

132 Overall, an unbiased whole-brain comparison of TH+ neuron counts revealed divergent
133 and dosage-dependent brain-wide impact of chronic ketamine exposure (**Fig. 1**) - increases within
134 multiple hypothalamic domains (e.g., ARH, containing TH+ DA neurons with orexigenic function
135 in energy homeostasis[40]) and decreases within the behavioral state related midbrain regions (e.g.,
136 DR, containing TH+ DA neuron which modulate the social isolation behaviors[37]; RR, containing
137 TH+ DA neurons with role in fear and aversive signaling[39]).

138 **Untranslated TH mRNA+ neurons facilitate ketamine-induced cellular plasticity**

139 We sought to further investigate the mechanistic basis of the chronic ketamine-induced
140 brain-wide cellular plasticity. Utilizing our whole-brain mRNA labeling protocol, we first mapped
141 the expression of TH mRNA (**Fig. 4a, Supplementary Video 4**), revealing a much broader
142 distribution than the corresponding TH protein. Such discrepancy in the TH mRNA/protein
143 expression (**Supplementary Video 5**) suggests a potential role for post-transcriptional
144 mechanisms in rapid modulation of the brain-wide DA system. To test this hypothesis further, we
145 utilized a well-characterized inducible TH-CreER transgenic line[32] (**Supplementary Fig. 2**),
146 crossed with a tdTomato reporter line, to investigate if the newly acquired TH+ neurons originated
147 from the untranslated TH mRNA+ neurons. TH-CreER induction (by 4-OHT i.p. injections) was
148 performed 1-week prior to the start of the ketamine exposure, thus, permanently labeling the pre-
149 treatment TH mRNA+ neurons by tdTomato. After 10 days of chronic ketamine (100 mg/kg)
150 exposure, the brains were harvested, cleared with passive CLARITY[34], and labeled with α-TH
151 antibody for a direct comparison of the after-treatment TH+ neurons with before-treatment TH
152 mRNA+ neurons, within the exact same brain samples. As shown in **Fig. 4b**, we found a significant
153 increase in TH protein+/tdTomato+ co-labeled neurons (α-TH ∩ tdTomato) in the ketamine-
154 treated group (compared to saline controls), while the overall number of tdTomato+ neurons

155 remained unchanged, consistent with unchanged TH mRNA+ neurons (**Fig. 4b**). Conversely, we
156 observed a decrease in TH protein+/tdTomato+ co-labeled neurons in the midbrain regions (which
157 showed reduction in TH+ DA neuron counts), while the tdTomato+ and TH mRNA+ neuron
158 counts remain unchanged compared to the saline controls (**Fig. 4c**). Altogether, these results
159 suggest that the cellular plasticity in the dopaminergic system may be facilitated by the existence
160 of a much larger pools of untranslated TH mRNA+ neurons to rapidly modulate the number of
161 available TH+ DA neurons in various regions of the brain.

162 **Altered long-range TH+ projections after chronic ketamine exposure**

163 Taking advantage of the high-resolution of our datasets, we sought to map the brain-wide
164 changes in TH+ neuronal projections. Note that TH+ neuronal projections may be DA or
165 noradrenergic, therefore they can only be inferred as catecholaminergic[28,29]. Using the suiteWB
166 pipeline, we estimated the projection densities in the ketamine (100 mg/kg, 10 days) treated and
167 saline control whole-brain datasets and performed a voxel-by-voxel (at 25x25x25 μm^3 sampling)
168 statistical comparisons across groups. As shown in **Fig. 5, Supplementary Video 6**, chronic
169 ketamine exposure resulted in robust brain-wide changes in TH+ projections. We observed
170 increased densities in multiple associative cortical regions including the prefrontal cortex (PFC)-
171 related prelimbic area (PL, **Supplementary Video 7, Fig. 5c**), orbital area (ORB, **Supplementary**
172 **Video 8, Fig. 5c**), frontal pole (FRP, **Fig. 5a**) and anterior cingulate area (ACA, **Fig. 5a**), and
173 posterior parietal association area (PTLp, **Fig. 5a**). Further, the lateral amygdala (LA,
174 **Supplementary Video 9, Fig. 5c**), which is crucial for processing of threatening stimuli and fear
175 behavior, specific regions of the lateral septal complex (septofimbrial nucleus (SF), involved in
176 reward and reinforcement) and the triangular nucleus of septum (TRS) also showed increased
177 projection densities (**Fig. 5a**). Furthermore, brain regions receiving olfactory inputs, including the
178 taenia tecta (TT) and piriform area (PIR), and regions of the thalamus (lateral posterior nucleus of
179 the thalamus (LP)) and hypothalamus (VMH and TU) also showed increases in the TH+ neuronal
180 innervations.

181 In contrast, the dorsal auditory area (AUDd, **Fig. 5d**, **Supplementary Video 10**), postero-
182 lateral visual area (VISpl, **Fig. 5d**, **Supplementary Video 11**), entorhinal area (ENT) and
183 presubiculum (PRE, involved in spatial information processing; **Fig. 5a**) exhibited decreased TH+
184 projection densities. Striatum sub-regions caudoputamen (Cp) and bed nuclei of the stria terminalis

185 (BST/BNST, **Fig. 5d**, **Supplementary Video 12**) showed reductions consistent with the loss of
186 TH+ neurons in DR, RR and SNc (**Fig. 3**). Finally, thalamic regions subparafascicular area (SPA)
187 and subparafascicular nucleus (SPF), and midbrain regions nucleus sagulum (SAG) and
188 pedunculopontine nucleus (PPN) also showed decreased projections.

189 Overall, consistent with the divergent changes in TH+ neuron counts in the midbrain and
190 hypothalamic dopaminergic domains (**Fig. 3**), chronic ketamine exposure resulted in increased
191 TH+ neuronal projection densities in the associative brain centers, including PFC-related regions,
192 and decreased innervations of visual, auditory, and spatial information processing regions (**Fig. 5**).

193 **DISCUSSION**

194 Utilizing an unbiased, high-resolution whole-brain mapping approach, we revealed
195 hitherto unknown divergence in the adaptability of the DA system to repeated ketamine exposure
196 (summarized in **Fig. 1b**) – reduced number of TH+ neurons within the behavior state-related mid-
197 brain domains and increased within the hypothalamic domains, along with altered long-range
198 innervation of the association and sensory areas by TH+ neuronal projections. Such structural
199 plasticity of brain-wide modulatory system may facilitate significant reconfiguration of the
200 neuronal networks in response to external stresses such as ketamine exposure or diseased
201 conditions (e.g., schizophrenia), to eventually result in long-lasting cognitive behavioral changes.
202 Note that, DA may further get processed in the noradrenergic neurons, but their cellular
203 distribution is well known to be restricted to specific domains in hindbrain regions[28,29]. However,
204 the TH+ neuronal projections may still not be precisely identified as DA or noradrenergic by TH
205 immunolabeling[28,29]. In addition, the loss of TH protein in DA neurons may not result in a
206 permanent loss of DA neurons, nevertheless, it does indicate the loss of DA producing capacity
207 due to the required role of TH in the L-DOPA (DA precursor) biosynthesis.

208 We also show that the adaptability of the DA system is facilitated by a large pool of neurons
209 that stably maintain translationally suppressed TH mRNA (**Fig. 4**). These findings were validated
210 by a direct comparison of the newly recruited or lost TH+ DA neurons with the before-exposure
211 TH mRNA expressing neuron populations by utilizing an inducible TH-CreER transgenic mice
212 line (**Fig. 4**). Mechanistically, these observed changes in DA system may, in part, be the result of
213 repeated ketamine-induced activation/deactivation (indirect, via NMDAR antagonism) of the DA
214 neurons due to the heterogeneous neuronal inputs. Intriguingly, the ketamine-induced cellular

plasticity is distinct from the previously reported neurotransmitter phenotypic plasticity of the hypothalamic DA neurons after changed day/night durations in rodents, and included loss of TH mRNA expression[42]. Overall, our data suggest that the maintenance of translationally suppressed mRNA, even though energetically costly process, may allow for faster brain-wide adaptations to various external stresses.

The development and use of unbiased, high-resolution whole-brain phenotyping of the entire DA system allowed discovery of the divergent impact of chronic ketamine exposure. Such non-monolithic brain-wide impact further underscores the need for unbiased investigations of on/off-target effects of ketamine treatment at a range of doses, as well as the urgency to develop targeted pharmacological intervention approaches (e.g., focused ultra sound-based approaches[43,44]) for treatment of complex brain disorders.

Acknowledgements

We are grateful to Jordan Hamm for critically reading the manuscript, and to Christine Denny, Rae Silver and Darcy Kelley for advice throughout the project. We thank Vivek Kumar for advice on the HCR probe design and general discussions. We are grateful to Briana Chen and Christine Denny for helping with the ANY-maze software. This work was supported by NIH grant DP2MH119423 and Columbia University Arts & Sciences startup grant to R.T.

Author Contributions

M.S.D., Y.C. and R.T. conceptualized and designed the project. M.S.D. performed most of the experiments. J.Z. performed mRNA staining experiments. E.D.D. contributed with animal husbandry and general experimental support. S.C. contributed to all the imaging experiments, and C.G. contributed to ClearScope imaging. Y.C. and R.T. developed the data analysis framework and code, and with M.S.D. analyzed the data. R.T., M.S.D. and Y.C. wrote the paper with inputs from all authors. R.T. supervised the project.

Data availability statement

All datasets will be made available on request.

Code availability

All code will be made available publicly as a GitHub repository.

Declaration of interests

The authors declare no competing interests.

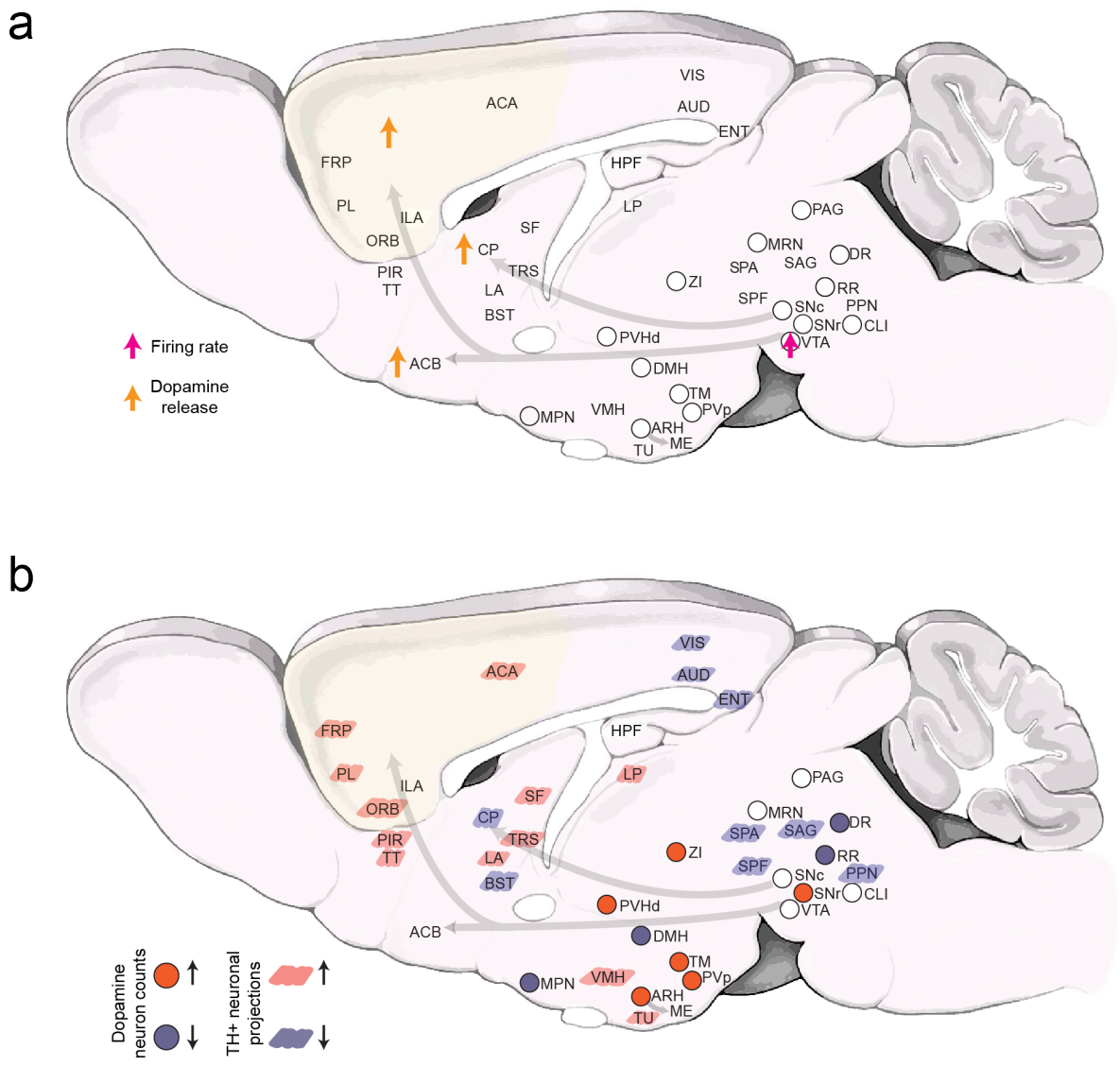

Figure 1. Brain-wide impact of ketamine exposure on the dopaminergic modulatory system. (a) Schematic summary of currently known alterations in dopaminergic neuronal activity and dopamine release after ketamine exposure[16,17]. (b) Schematic summary (this study) of the brain-wide alterations in the DA system after 10 days of repeated ketamine (30 and 100 mg/kg) exposure. Up and down arrows indicate increase and decrease, respectively. Note that, for the 30 mg/kg ketamine treatment, statistically significant decreases in TH+ neuron counts were only observed in DR, DMH and MPN, and increase in ZI. The TH+ neuronal projections changes are only shown for the 100 mg/kg (10 days) treatment. Abbreviations used are standard Allen Brain Atlas terms,

as follows. ACA: anterior cingulate area; ACB: nucleus accumbens; ARH: arcuate hypothalamic nucleus; AUD: auditory areas; BST: bed nuclei of the stria terminalis; CLI: central linear nucleus raphe; CP: caudoputamen; DMH: dorsomedial nucleus of the hypothalamus; DR: dorsal nucleus raphe; ENT: entorhinal area; FRP: frontal pole, cerebral cortex; HPF: hippocampal formation; IF: interfascicular nucleus raphe; ILA: infralimbic area; LA: lateral amygdalar nucleus; LP: lateral posterior nucleus of the thalamus; MPN: medial preoptic nucleus; MRN: midbrain reticular nucleus; ORB: orbital area; PAG: periaqueductal gray; PIR: piriform area; PL: prelimbic area; PPN: pedunculopontine nucleus; PVH: paraventricular hypothalamic nucleus; PVp: paraventricular hypothalamic nucleus, posterior part; RR: midbrain reticular nucleus, retrorubral area; SAG: nucleus sagulum; SF: septofimbrial nucleus; SNc: substantia nigra, compact part; SPA: subparafascicular area; SPF: subparafascicular nucleus; TM: tuberomammillary nucleus; TRS: triangular nucleus of septum; TT: taenia tecta; TU: tuberal nucleus; VIS: visual areas; VMH: ventromedial hypothalamic nucleus; VTA: ventral tegmental area; ZI: zona incerta.

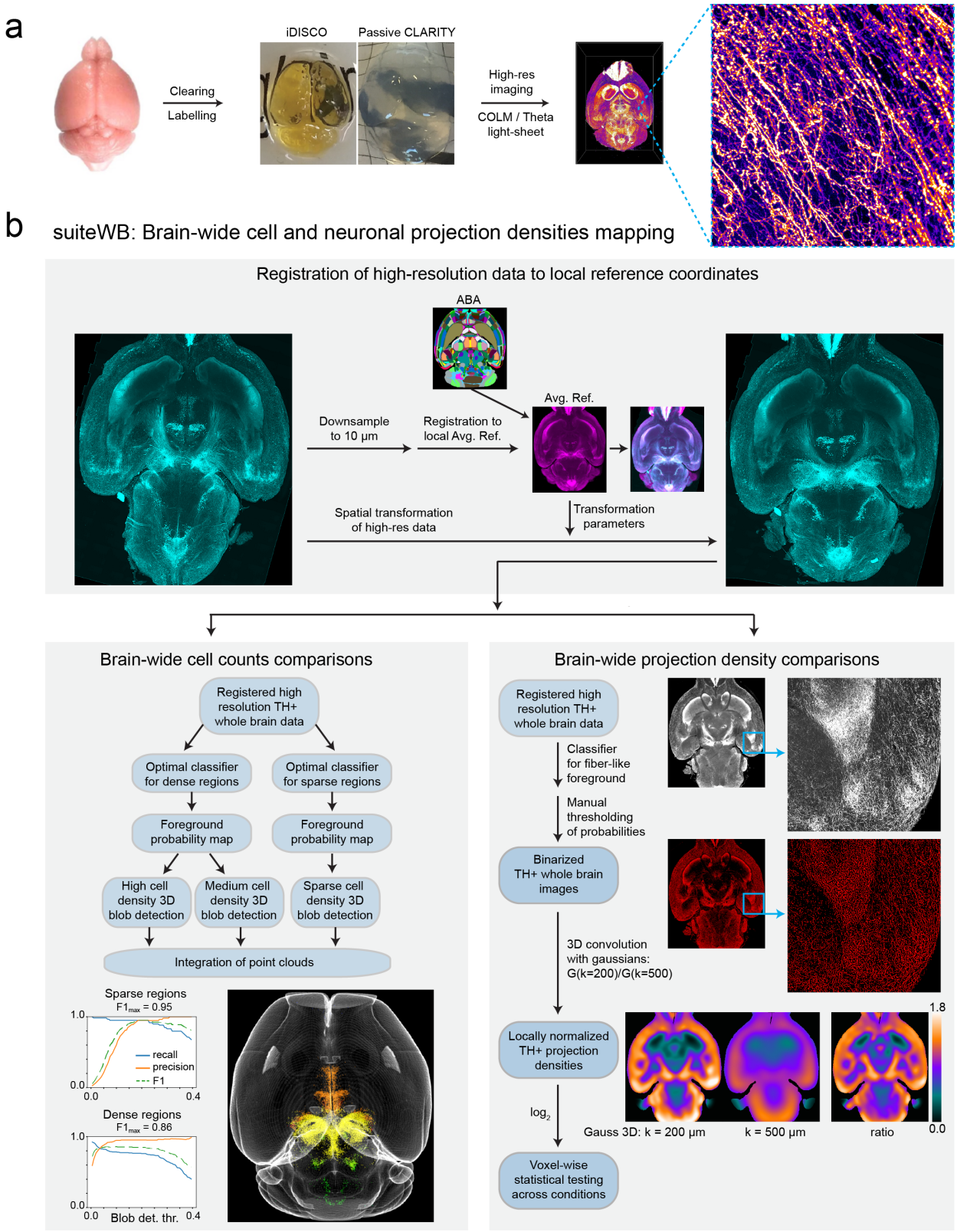

Figure 2. High-resolution whole-brain phenotyping of dopaminergic modulatory system. (a) Whole brain mapping of TH+ neurons by optimized labelling (α-TH antibody staining, TH mRNA

staining and/or TH-CreER x tdTomato signal), clearing (iDISCO+ or passive CLARITY) and high-resolution imaging with COLM or LSTM light sheet microscopy. (b) A suite of tools (suiteWB) for high-resolution comparative phenotyping of neuron counts and their brain-wide projection, including registration of high-resolution whole-brain images to a local average reference brain (with mapped ABA reference annotations), accurate brain-wide multi-model cell segmentation approach and neuronal projections density estimation. F1 for sparse and dense region segmentations achieved are 0.95 and 0.86, respectively. Also see **Supplementary Videos 1-4** for volume renderings of the raw data and segmentation results.

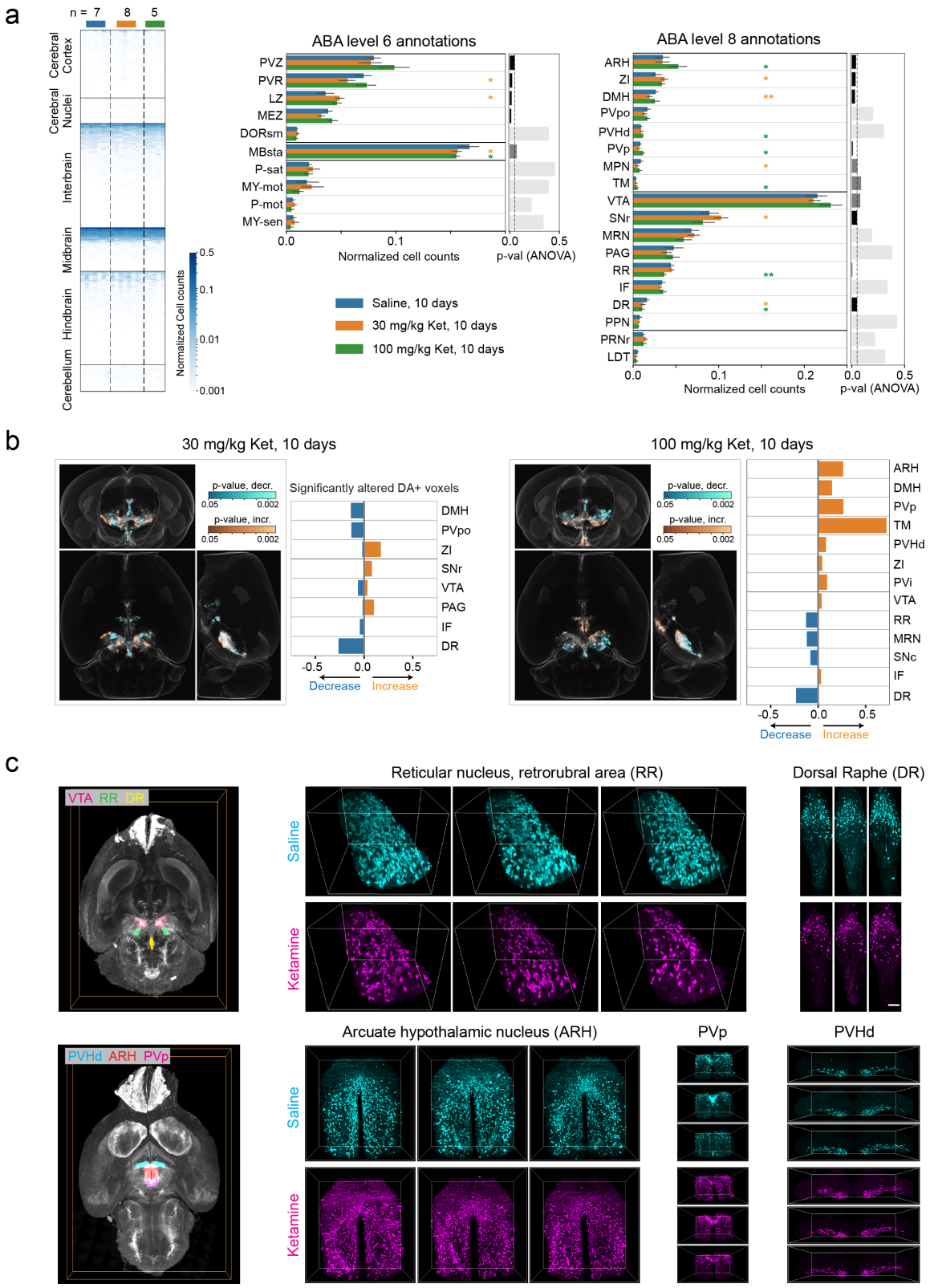

Figure 3. Repeated ketamine exposure results in divergent brain-wide changes in the dopaminergic modulatory system. (a) Brain-wide heatmap of the TH+ cell counts in ABA ROIs

after 10 days ketamine (30 mg/kg and 100 mg/kg) and saline (Sal) i.p. injections. Independent biological replicates of n=7 for Sal, 8 for 30 mg/kg ketamine and 5 for 100 mg/kg ketamine treated groups. The regional TH+ neuron counts were normalized by respective total number of TH+ neurons in brain. Orange, green, and blue bars quantify TH+ cells in 30 mg/kg ketamine, 100 mg/kg ketamine and saline-treated brains, respectively. Two-sided Mann-Whitney U tests with Bonferroni Correction were performed to calculate the statistical significance. * and ** indicate p-values < 0.05 and < 0.01, respectively. ANOVA tests p-values are plotted as bar plots on the right. (b) Whole brain orthogonal projections visualizing voxel-by-voxel differences in TH+ neuron densities after 10 days of 30mg/kg ketamine (n=8) and 100mg/kg ketamine (n=5), compared with saline (n=7) controls. Cyan and Orange visualize p-values (two-sided Mann-Whitney U test) for decreases and increases, respectively. Note that the decreases and increases in the densities are identified by comparing the sample averages of the treated and control groups. The bar plots quantify the fraction of DA neurons containing voxels (within an ABA ROI) that show significant alterations. (c) Representative volume renderings from 3 different brain samples, each for ketamine (100 mg/kg, 10 days) and saline samples, showing decreases in RR (Reticular nucleus, retrorubral area) and DR (Dorsal raphe), and increases in ARH (Arcuate hypothalamic nucleus), PVp (Periventricular hypothalamic nucleus, posterior part) and PVHd (Periventricular hypothalamic nucleus, descending division). Renderings on the left visualize the spatial locations of these regions in the brain.

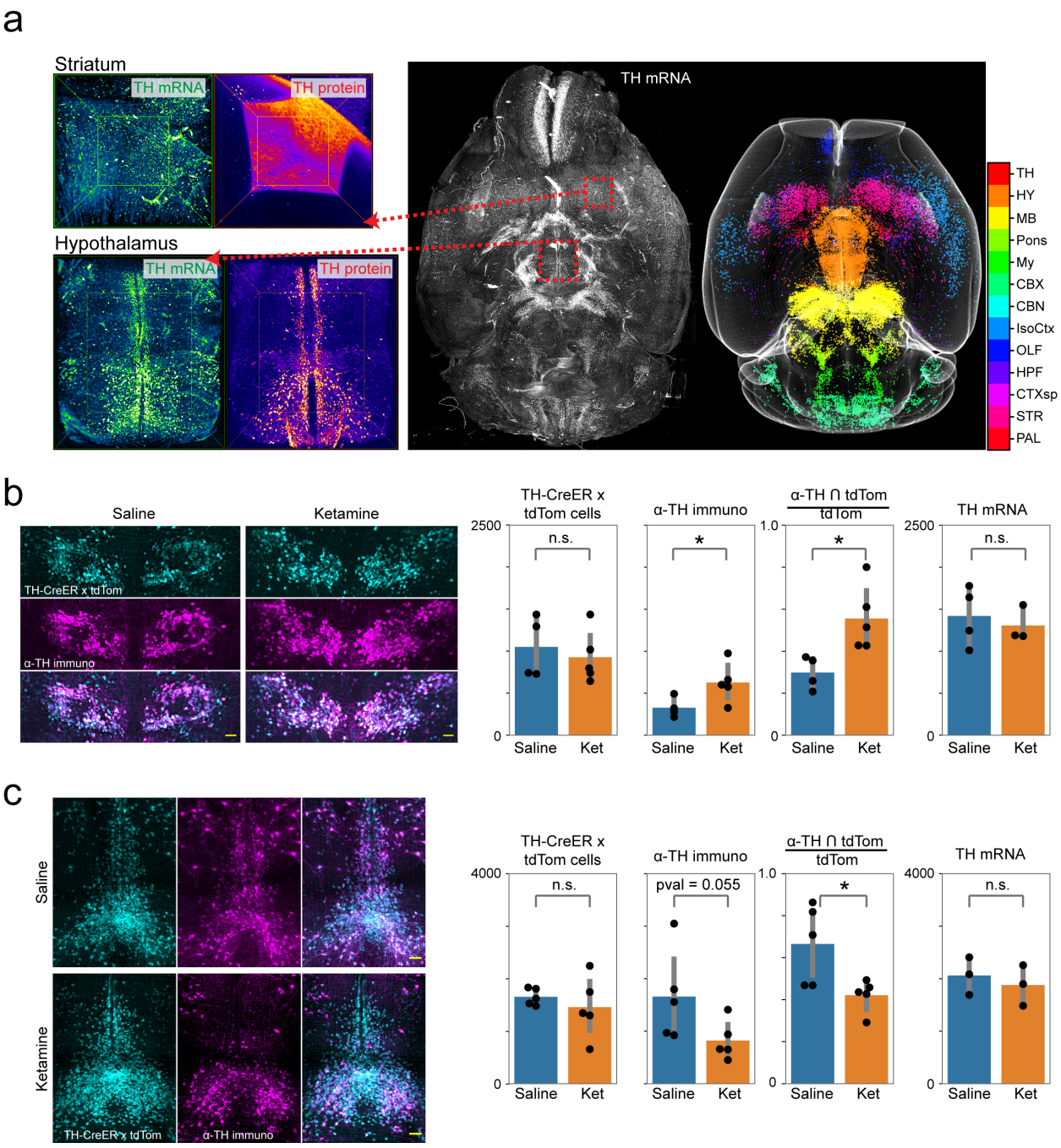

Figure 4. Untranslated TH mRNA+ neurons facilitate adaptations in the dopamine system. (a) Whole brain mapping of TH mRNA, showing much broader expression than the TH protein. Color code corresponds to different ABA ROIs, as listed in adjoining color bar. (b-c) Co-labeling of TH-CreER x tdTomato signal induced with 4-OHT injections one week before the start of ketamine i.p. injections and α-TH immunostaining signal capturing TH protein expression post-treatment (10 days). Left to right, bar plots compare the number of tdTomato+ neurons, α-TH

312 immunostained neurons, their intersection and the number of TH mRNA+ neurons. (b) and (c)
313 show field-of-views that include paraventricular hypothalamic nucleus and dorsal raphe regions,
314 respectively. Two-sided Mann-Whitney U tests were performed for statistical significance
315 calculations. * indicates <0.05 p-value. All scale bars are 100 µm. Also see **Supplementary**
316 **Videos 4** and **5** for whole brain volumetric renderings.

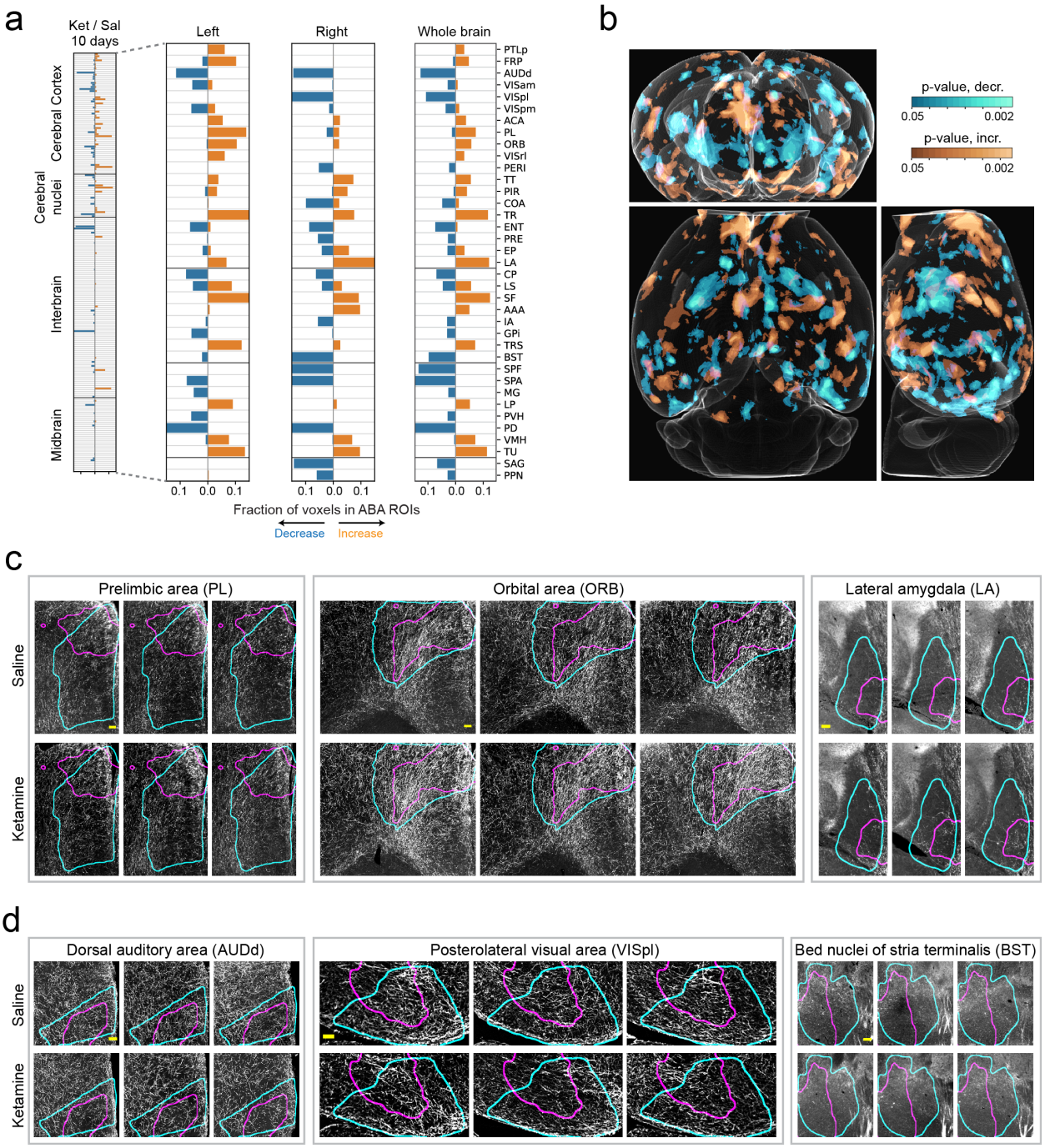

Figure 5. Brain-wide changes in TH+ neuronal projections after chronic ketamine exposure. (a) Stacked barplots of fractions of ABA ROI voxels with significantly increased (orange) and decreased (blue) TH+ neuronal projection densities after 10 days of ketamine exposure. Independent biological replicates as follows: n (Ket, 10d) = 5, n (Sal, 10d) = 7. (b) Whole brain orthogonal projections visualizing voxel-by-voxel differences (independent of ABA) in TH+ neuronal projection densities. Orange and Cyan represent significant increases and decreases,

respectively. (c-d) Representative examples of ABA ROIs showing increases (c) and decreases (d) in TH+ neuronal projections. Cyan and Magenta curves outline the ABA ROIs and areas with significantly changed projection densities. Images shown are representative single optical planes. Also see **Supplementary Video 6** for rendering of heatmaps, **Supplementary Videos 7-12** for complete volumes. All scale bars are 100 μm.

329 **Methods**

330 ***Animals.*** Male TH-2a-CreER[32] mice were acquired from Dr. David Ginty's lab and were bred
331 with B6;129S6-*Gt(ROSA)26Sor*$^{tm14(CAG\text{-}tdTomato)Hze}$/J (Ai14; JAX Strain #:007908). All mice were
332 group-housed in a 12:12 light:dark cycle at 22ºC. Food and water were provided *ad libitum. (R,S)-*
333 ketamine i.p. injections were performed during the light phase. All experimental procedures were
334 approved by the IACUC at Columbia University. Locomotor activity was recorded after 1, 5, and
335 10 days of treatment. The mice were placed within a novel home cage and were recorded (camera:
336 GoHZQ, 1920 x 1080 pixels,30 fps transmission rate) 15 minutes and 1 hour post- intraperitoneal
337 ketamine injections. The total distance traveled was quantified using the ANY-maze tracking
338 software (ANY-maze, RRID:SCR_014289, Stoelting, Wood Dale, IL, United States).

339 ***Drugs.*** 4-hydroxytamoxifen (4-OHT; Sigma, H7904) was dissolved in corn oil/ethanol (90% corn
340 oil, 10% ethanol) via the use of a vortex, ultrasonication, and 55°C heating for <15 min. Mice were
341 intraperitoneally injected with 2 mg of 4-OHT. *(R,S)*-ketamine (Covetrus) was used for all
342 ketamine exposure experiments. 3 and 10 mg/mL stocks were prepared in saline (0.9% NaCl)[45].
343 One dose of 30 mg/kg or 100 mg/kg of *(R,S)*-ketamine was intraperitoneally injected in a 24 hour
344 period for 1 day, 5 days, or 10 days treated animals. 8-10 weeks old mice were used for all
345 experiments.

346 ***Whole brain clearing and labelling.*** For iDISCO clearing, the iDISCO+ protocol was followed
347 as previously described[33]. The brains were pre-treated with methanol, placed in 66%
348 dichloromethane/ 33% methanol overnight, bleached with 5% H_2O_2/methanol, and then
349 rehydrated. Afterwards, the whole brains were permeabilized for 2 days at 37°C in 1x phosphate
350 buffered saline (PBS), 0.2% Triton X-100, 0.3 M glycine, and 20% dimethyl sulfoxide (DMSO).
351 The brains were blocked with 1xPBS, 0.2% Triton X-100, 10% DMSO, 6% donkey serum for 2
352 days at 37°C, followed by incubation in 1xPBS, 0.1% Triton X-100, 3% donkey serum, and a
353 1:200-1:500 dilution of the primary antibody sheep α-TH (ab113, Abcam) for 10 days. After
354 washing in 1xPBS/0.1% Triton X-100, the brains were placed in the secondary antibody solution
355 containing 1xPBS/0.1% Triton X-100/3% donkey serum and a 1:1000 dilution of donkey anti-
356 sheep 647 (A-21448, Thermofisher) for 10 days.

357 We used the passive CLARITY method as detailed previously[34]. The tissue was first
358 encapsulated in a hydrogel monomer (HM) solution consisting of 1% (wt/vol) acrylamide, 0.05%

359 (wt/vol) bisacrylamide, 4% paraformaldehyde, 1x phosphate buffered saline (1xPBS), deionized
360 water, and 0.25% of thermal initiator (VA-044, Fisher Scientific), followed by clearing with SBC
361 buffer (4% (wt/vol) SDS, 0.2 M boric acid, pH 8.5 and deionized water) at 37°C with shaking. The
362 SBC buffer was replaced every 2 days. After clearing, the SBC buffer was washed off with 0.2 M
363 boric acid pH 8.5 with 0.1% Triton X-100. The cleared tissue was immunostained in 0.2 M boric
364 acid pH 7.5 with 0.1% Triton X-100. The final refractive index matching was performed in
365 RapiClear (SunJin lab, RI=1.47).

366 For HCR-FISH, we used split-initiator DNA probes (IDT) for detecting the tyrosine
367 hydroxylase (Th, NM_012740.3) mRNA. During probe hybridization/detection, the brains
368 underwent 1) equilibration with 5xSSCTw buffer, 2) acetylation with 0.25% acetic anhydride
369 solution, 3) equilibration with probe hybridization buffer (30% formamide, 5xSSC, 0.5 mg/mL
370 yeast tRNA, 10% dextran sulfate), and 4) probe incubation (50 nM) in probe hybridization buffer
371 at 37C. The time/amount of solution varied depending on the thickness of the brain slices. The
372 slices were then washed in probe wash buffer (30% formamide, 5X SSC, 9 mM citric acid, and
373 0.1% tween 20) at 37ºC as well as two rounds of washes in 5xSSCTw. Afterwards, the slices were
374 equilibrated in amplification buffer (5xSSC, 10% dextran sulfate, and 0.1% Tween-20), and then
375 incubated in amplification buffer with 50-150 nM of hairpins H1 and H2 conjugated with AF-647
376 (Molecular Instruments). The hairpin/amplification buffer mixture was then washed off with
377 several rounds of 5xSSCTw.

378 For activated caspase staining, the TH-2a-CreER;Ai14 brains were sliced with a vibratome
379 (Leica VT1000 S Vibrating blade microtome) into 50 μm sections. These sections were placed in
380 a blocking buffer (1xPBS/0.1% bovine serum albumin/0.1% Triton X-100) for 30 minutes and
381 then incubated in a 1:200-1:400 dilution of the primary antibody, rabbit anti-active caspase-3 (BD
382 Biosciences, catalog no. 559565), with 1xPBS/0.5% bovine serum albumin /0.1% Triton X-100
383 overnight. After washing in 1xPBS/0.1% Triton X-100, the sections were incubated, for two hours,
384 in a 1:500 dilution of the secondary antibody, goat anti-rabbit 647 (ThermoFisher, Catalog #A-
385 21245) with 1xPBS/0.5% bovine serum albumin /0.1% Triton X-100. The secondary antibody was
386 washed off in 1xPBS/0.1% Triton X-100, and the slices were incubated in a 1:1000 dilution of a 1
387 mg/mL stock of DAPI with 1xPBS for 15 minutes. After washing off with 1xPBS/0.1% Triton X-
388 100, the slices were mounted in 65% glycerol.

389 ***Imaging.*** All imaging experiments were performed with CLARITY-optimized light sheet
390 microscopy (COLM)[34] or ClearScope (MBF Biosciences)[35] Olympus 10x/0.6NA/8 mmWD or
391 ASI 16x/12mmWD detection objectives were used for most of the whole brain imaging with
392 COLM. Olympus Macro 4×/0.28NA or Nikon 20x/1.0NA were used for ClearScope imaging.

393 ***suiteWB: Image Registration.*** We first developed a fast and efficient multistep multiresolution
394 3D image registration tool by using Mutual Information[46] as the similarity metric. The registration
395 starts by rigid transformation (with 6 degrees of freedom for rotation and translation) of the moving
396 image (i.e. the image being aligned) to roughly align with the reference image. Next, the moving
397 image is affine transformed (12 degrees of freedom) to account for shearing and shrinking artifacts
398 introduced by labeling, tissue clearing and imaging. Finally, we used a uniform grid of control
399 points and third-order B-splines are used for non-rigid local transformations. Affine and nonrigid
400 steps were done at three different resolutions. The algorithms were implemented with ITKv4[47]
401 registration framework. All α-TH stained whole brain images were registered at 10 μm resolution
402 to a local average reference brain (generated from 7 α-TH whole brain images), and the resulting
403 spatial transformation parameters were applied to high-resolution datasets. ABA annotations were
404 registered one time to the local average reference brain.

405 ***suiteWB: Multi-model segmentation pipeline.*** Segmentation of whole brain images presents
406 unique challenges of high spatial variations in signal-noise ratios (SNR), object densities and
407 varied image artifacts. Multiple open-source tools exist for cell segmentation[48–50], however, some
408 of them are optimized for confocal images with smaller data sizes, others utilize deep learning
409 models with pre-trained parameters that do not accurately generalize to images with different
410 signal quality distribution and also require dense annotation training datasets. We chose to develop
411 a semi-supervised multi-model learning approach to address the challenges of whole brain
412 segmentation. This approach does not require dense annotated training and also allows the
413 flexibility of using different optimal parameter sets for different regions (i.e. with dense or sparse
414 object densities). We utilized open-source toolkit ilastik[51] for semi-supervised learning of
415 classifiers based on image features.

416 The high-resolution registered whole brain images were split into densely and sparsely
417 populated regions by visual inspection, followed by pixel classification to generate probability
418 maps. For the sparse region, a standard pixel classification workflow in ilastik was applied to

generate cell probability maps. First, image features were extracted by using multiple types of filters with different kernel sizes, including intensity filters (Gaussian Smoothing), edge detection filters (Laplacian of Gaussian, Gaussian Gradient Magnitude, Difference of Gaussians), and texture detection filters (Structure Tensor Eigenvalues, Hessian of Gaussian Eigenvalues). The image features were then used to estimate the probabilities of pixels belonging to a cell or background. For denser regions, we utilized the Autocontext workflow in ilastik. In the first step, the image pixels were classified into five categories: empty space, brain background, fibers (neuronal projections), cell cytoplasm and cell nucleus. In the second step, the classification results were combined with image features (with filters described above for sparse regions) to generate probability maps of cells against background. Next, we applied blob detection on the dense and sparse probability maps separately to detect cells. This was achieved by using the difference of Gaussian (DOG) algorithm (Python scikit-image package[52]. To optimize memory usage, images were processed block-wise with carefully resolved boundary conditions. Cells detected in dense and sparse regions were merged and were further tuned by using Napari viewer. F1 for sparse and dense region segmentations reached 0.95 and 0.86, with precision 0.889 and 0.976 respectively, compared to human-annotated datasets (**Fig. 2**). For comparison, ClearMap[48], applied to immediate early gene datasets, reported a precision of 0.83 and 0.75 compared to two human annotators.

For colocalization analysis of the multi-channel (i.e. tdTomato and α-TH immunostaining signal) CLARITY images, cell detection (as described above) was applied separately to different channels. The full cell body labels were generated by taking the union of the detected cells in the two channels that were less than 25μm apart. The cell identities (i.e. if expressing tdTomato or α-TH or both) were assigned by manually validated thresholding of probability maps of each channel.

Neuronal projection segmentation was performed by semi-supervised pixel classification by using image features (as discussed above) to generate the probability maps distinguishing projections and background. The probability threshold for binarization was determined by careful inspection throughout various regions of the brain. The binarized data was then convolved with 3D Gaussian kernels of 200 μm and 500 μm. The ratio of the two gaussians resulted in locally normalized neuronal projection densities.

Statistical comparisons between Ketamine and Saline treated samples were done with two-sided Mann Whitney U test (using Python package Scipy[53]) on normalized cell counts (cell count in a region divided by total cell count of that whole brain) and cell densities (estimated by 3D Gaussian kernel of size 50 μm in each dimension).

453 **References**

454 1. Bell, R. F. & Kalso, E. A. Ketamine for pain management. *Pain Rep* **3**, e674 (2018).

455 2. Berman, R. M. *et al.* Antidepressant effects of ketamine in depressed patients. *Biological*
456 *Psychiatry* **47**, 351–354 (2000).

457 3. Ibrahim, L. *et al.* Course of Improvement in Depressive Symptoms to a Single Intravenous
458 Infusion of Ketamine vs Add-on Riluzole: Results from a 4-Week, Double-Blind, Placebo-Controlled
459 Study. *Neuropsychopharmacol* **37**, 1526–1533 (2012).

460 4. Zarate, C. A. *et al.* A randomized trial of an N-methyl-D-aspartate antagonist in treatment-
461 resistant major depression. *Arch Gen Psychiatry* **63**, 856–864 (2006).

462 5. Daly, E. J. *et al.* Efficacy and Safety of Intranasal Esketamine Adjunctive to Oral Antidepressant
463 Therapy in Treatment-Resistant Depression: A Randomized Clinical Trial. *JAMA Psychiatry* **75**, 139–148
464 (2018).

465 6. Zanos, P. *et al.* NMDAR inhibition-independent antidepressant actions of ketamine metabolites.
466 *Nature* **533**, 481–486 (2016).

467 7. Zanos, P. *et al.* Ketamine and Ketamine Metabolite Pharmacology: Insights into Therapeutic
468 Mechanisms. *Pharmacol Rev* **70**, 621–660 (2018).

469 8. Olney, J. W., Newcomer, J. W. & Farber, N. B. NMDA receptor hypofunction model of
470 schizophrenia. *Journal of Psychiatric Research* **33**, 523–533 (1999).

471 9. Franks, N. P. & Lieb, W. R. Molecular and cellular mechanisms of general anaesthesia. *Nature*
472 **367**, 607–614 (1994).

473 10. Chen, X., Shu, S. & Bayliss, D. A. HCN1 Channel Subunits Are a Molecular Substrate for Hypnotic
474 Actions of Ketamine. *J. Neurosci.* **29**, 600–609 (2009).

475 11. Zhou, C. *et al.* Forebrain HCN1 channels contribute to hypnotic actions of ketamine.
476 *Anesthesiology* **118**, 785–795 (2013).

477 12. Sleigh, J., Harvey, M., Voss, L. & Denny, B. Ketamine – More mechanisms of action than just
478 NMDA blockade. *Trends in Anaesthesia and Critical Care* **4**, 76–81 (2014).

479 13. Gupta, A., Devi, L. A. & Gomes, I. Potentiation of μ-opioid receptor-mediated signaling by
480 ketamine. *Journal of Neurochemistry* **119**, 294–302 (2011).

481 14. Moda-Sava, R. N. *et al.* Sustained rescue of prefrontal circuit dysfunction by antidepressant-
482 induced spine formation. *Science* **364**, eaat8078 (2019).

483 15. Cichon, J. *et al.* Ketamine triggers a switch in excitatory neuronal activity across neocortex. *Nat*
484 *Neurosci* (2022) doi:10.1038/s41593-022-01203-5.

485 16. Kokkinou, M., Ashok, A. H. & Howes, O. D. The effects of ketamine on dopaminergic function:
486 meta-analysis and review of the implications for neuropsychiatric disorders. *Mol Psychiatry* **23**, 59–69
487 (2018).

488 17. Simmler, L. D. *et al.* Dual action of ketamine confines addiction liability. *Nature* 1–6 (2022)
489 doi:10.1038/s41586-022-04993-7.

490 18. Iro, C. M., Hamati, R., El Mansari, M. & Blier, P. Repeated but Not Single Administration of
491 Ketamine Prolongs Increases of the Firing Activity of Norepinephrine and Dopamine Neurons. *Int J*
492 *Neuropsychopharmacol* **24**, 570–579 (2021).

493 19. Smith-Apeldoorn, S. Y., Veraart, J. K., Spijker, J., Kamphuis, J. & Schoevers, R. A. Maintenance
494 ketamine treatment for depression: a systematic review of efficacy, safety, and tolerability. *The Lancet*
495 *Psychiatry* **9**, 907–921 (2022).

496 20. Short, B., Fong, J., Galvez, V., Shelker, W. & Loo, C. K. Side-effects associated with ketamine use
497 in depression: a systematic review. *The Lancet Psychiatry* **5**, 65–78 (2018).

498 21. Morgan, C. J. A., Curran, H. V. & Drugs (ISCD), the I. S. C. on. Ketamine use: a review. *Addiction*
499 **107**, 27–38 (2012).

500 22. Ke, X. *et al.* The profile of cognitive impairments in chronic ketamine users. *Psychiatry Research*
501 **266**, 124–131 (2018).

502 23. Zhang, C., Xu, Y., Zhang, B., Hao, W. & Tang, W. K. Cognitive impairment in chronic ketamine
503 abusers. *Psychiatry Research* **291**, 113206 (2020).

504 24. Strous, J. F. M. *et al.* Brain Changes Associated With Long-Term Ketamine Abuse, A Systematic
505 Review. *Front. Neuroanat.* **16**, 795231 (2022).

506 25. Behrens, M. M. *et al.* Ketamine-Induced Loss of Phenotype of Fast-Spiking Interneurons Is
507 Mediated by NADPH-Oxidase. *Science* **318**, 1645–1647 (2007).

508 26. Hamm, J. P., Peterka, D. S., Gogos, J. A. & Yuste, R. Altered Cortical Ensembles in Mouse Models
509 of Schizophrenia. *Neuron* **94**, 153-167.e8 (2017).

510 27. Garritsen, O., van Battum, E. Y., Grossouw, L. M. & Pasterkamp, R. J. Development, wiring and
511 function of dopamine neuron subtypes. *Nat Rev Neurosci* 1–19 (2023) doi:10.1038/s41583-022-00669-3.

512 28. Hussain, L. S., Reddy, V. & Maani, C. V. Physiology, Noradrenergic Synapse. in *StatPearls*
513 (StatPearls Publishing, 2023).

514 29. Robertson, S. D., Plummer, N. W., de Marchena, J. & Jensen, P. Developmental origins of central
515 norepinephrine neuron diversity. *Nat Neurosci* **16**, 1016–1023 (2013).

516 30. Dirks, R. M. & Pierce, N. A. Triggered amplification by hybridization chain reaction. *Proceedings*
517 *of the National Academy of Sciences* **101**, 15275–15278 (2004).

518 31. Kumar, V. *et al.* Optimization and evaluation of fluorescence in situ hybridization chain reaction
519 in cleared fresh-frozen brain tissues. *Brain Struct Funct* **226**, 481–499 (2021).

520 32. Abraira, V. E. *et al.* The Cellular and Synaptic Architecture of the Mechanosensory Dorsal Horn.
521 *Cell* **168**, 295-310.e19 (2017).

522 33. Renier, N. *et al.* iDISCO: a simple, rapid method to immunolabel large tissue samples for volume
523 imaging. *Cell* **159**, 896–910 (2014).

524 34. Tomer, R., Ye, L., Hsueh, B. & Deisseroth, K. Advanced CLARITY for rapid and high-resolution
525 imaging of intact tissues. *Nature Protocols* **9**, 1682–1697 (2014).

526 35. Migliori, B. *et al.* Light sheet theta microscopy for rapid high-resolution imaging of large
527 biological samples. *BMC Biology* **16**, 57 (2018).

528 36. Wang, Q. *et al.* The Allen Mouse Brain Common Coordinate Framework: A 3D Reference Atlas.
529 *Cell* **181**, 936-953.e20 (2020).

530 37. Matthews, G. A. *et al.* Dorsal Raphe Dopamine Neurons Represent the Experience of Social
531 Isolation. *Cell* **164**, 617–631 (2016).

532 38. Moriya, S. *et al.* Involvement of A13 dopaminergic neurons located in the zona incerta in
533 nociceptive processing: a fiber photometry study. *Molecular Brain* **13**, 60 (2020).

534 39. Moaddab, M. & McDannald, M. A. Retrorubral field is a hub for diverse threat and aversive
535 outcome signals. *Current Biology* **31**, 2099-2110.e5 (2021).

536 40. Zhang, X. & van den Pol, A. N. Hypothalamic arcuate nucleus tyrosine hydroxylase neurons play
537 orexigenic role in energy homeostasis. *Nat Neurosci* **19**, 1341–1347 (2016).

538 41. Dominguez, J. M. & Hull, E. M. Dopamine, the medial preoptic area, and male sexual behavior.
539 *Physiology & Behavior* **86**, 356–368 (2005).

540 42. Dulcis, D., Jamshidi, P., Leutgeb, S. & Spitzer, N. C. Neurotransmitter Switching in the Adult Brain
541 Regulates Behavior. *Science* **340**, 449–453 (2013).

542 43. Ozdas, M. S. *et al.* Non-invasive molecularly-specific millimeter-resolution manipulation of brain
543 circuits by ultrasound-mediated aggregation and uncaging of drug carriers. *Nat Commun* **11**, 4929
544 (2020).

545 44. Pouliopoulos, A. N. *et al.* A Clinical System for Non-invasive Blood–Brain Barrier Opening Using a
546 Neuronavigation-Guided Single-Element Focused Ultrasound Transducer. *Ultrasound in Medicine and*
547 *Biology* **46**, 73–89 (2020).

548 45. Brachman, R. A. *et al.* Ketamine as a prophylactic against stress-induced depressive-like
549 behavior. *Biol Psychiatry* **79**, 776–786 (2016).

550 46. Viola, P. & Wells III, W. M. Alignment by Maximization of Mutual Information. *International*
551 *Journal of Computer Vision* **24**, 137–154 (1997).

552 47. McCormick, M., Liu, X., Jomier, J., Marion, C. & Ibanez, L. ITK: enabling reproducible research
553 and open science. *Front Neuroinform* **8**, 13 (2014).

554 48. Renier, N. *et al.* Mapping of Brain Activity by Automated Volume Analysis of Immediate Early
555 Genes. *Cell* **165**, 1789–1802 (2016).

556 49. Tyson, A. L. *et al.* A deep learning algorithm for 3D cell detection in whole mouse brain image
557 datasets. *PLOS Computational Biology* **17**, e1009074 (2021).

558 50. Stringer, C., Wang, T., Michaelos, M. & Pachitariu, M. Cellpose: a generalist algorithm for cellular
559 segmentation. *Nat Methods* **18**, 100–106 (2021).

560 51. Berg, S. *et al.* ilastik: interactive machine learning for (bio)image analysis. *Nat Methods* **16**,
561 1226–1232 (2019).

562 52. Walt, S. van der *et al.* scikit-image: image processing in Python. *PeerJ* **2**, e453 (2014).

563 53. Virtanen, P. *et al.* SciPy 1.0: fundamental algorithms for scientific computing in Python. *Nat*
564 *Methods* **17**, 261–272 (2020).

565

566